Merging galaxy clusters: probing magnetism and particle acceleration over cosmic time

Di Gennaro, G.

Author: Di Gennaro, G.
Title: Merging galaxy clusters: probing magnetism and particle acceleration over cosmic time
Issue date: 2021-07-08

CHAPTER

6

A LOFAR-UGMRT SPECTRAL INDEX STUDY OF DISTANT RADIO HALOS

G. Di Gennaro, R.J. van Weeren, R. Cassano, G. Brunetti, M. Brüggen et al. *Astronomy & Astrophysics*, to be submitted.

Abstract. Radio halos are Mpc-scale diffuse radio sources located at the centres of merging galaxy clusters. The common mechanism invoked to explain their origin is the re-acceleration of relativistic particles driven by large-scale turbulence. Current re-acceleration models predict that a significant number of halos at high redshift should be characterised by very steep spectra ($\alpha < -1.5$), due to strong Inverse Compton energy losses. In this paper, we investigate the spectral index properties of a sample of nine clusters selected from the second Planck Sunyaev-Zel'dovic catalogue showing diffuse radio emission with the Low Frequency Array (LOFAR) in the 120–168 MHz band. We analysed upgraded Giant Metrewave Radio Telescope (uGMRT) observations in Band 3 and 4, i.e. 250–500 and 550-900 MHz respectively. These observations were combined with existing LOFAR data to produce spectral index maps and to retrieve the cluster spectral properties.We find diffuse radio emission in the uGMRT observations for five of the nine high-z radio halos previously discovered with LOFAR. For those, we measure spectral indices in the range of -1 to -1.4. For the uGMRT non-detections, we estimated upper limits on the spectral index of < -1.5. We also find only one candidate relic. Despite the poor statistics, we find evidence that a significant fraction of massive and merging clusters at high redshift host radio halos with very steep spectra. This is consistent with theoretical predictions, although larger statistical samples are necessary to test models.

6.1. Introduction

In the framework of the ΛCDM cosmological model, galaxy clusters form and grow via accretion of less massive systems (e.g. galaxy groups or small galaxy clusters, see Press & Schechter, 1974; Springel et al., 2006). These events release up to 10^{64} erg in the intracluster medium (ICM) in a few Gyrs. A fraction of this energy is dissipated by shocks and turbulence into the amplification of magnetic fields and (re)acceleration of particles, producing diffuse radio emission in the form of *radio halos* and *radio relics* (see Brunetti & Jones, 2014; van Weeren et al., 2019, for recent theoretical and observational reviews). Due to their intrinsic low surface brightness (~ 1 μJy arcsec^{-2} at 1.4 GHz), halos and relics are difficult to detect. In addition, they are characterised by steep spectra (i.e. $\alpha < -1$, with $S_\nu \propto \nu^\alpha$), hence they are better observed at low radio frequencies (i.e. below GHz).

Radio halos are cluster-size structures that generally follow the distribution of the thermal cluster emission (i.e. the ICM). Their currently favoured formation scenario involves the re-acceleration of electrons via turbulence induced by cluster merger events (e.g. Brunetti et al., 2001; Petrosian, 2001; Donnert et al., 2013). In support of this scenario, radio halos are preferentially detected in dynamically disturbed clusters. The non-detection of γ-rays emission from galaxy clusters, at the level expected (e.g. Reimer et al., 2003; Ackermann et al., 2010a; Prokhorov & Churazov, 2014b; Brunetti et al., 2017; Adam et al., 2021), strongly disfavours hadronic models. The results of proton-proton collisions can generate secondary electrons which then emit synchrotron radiation (e.g. Brunetti & Lazarian, 2011; Pinzke et al., 2017; Brunetti et al., 2017)

Radio relics are elongated structures, generally located in the cluster outskirts. It is widely believed that these are associated with propagating shock waves caused by mergers (e.g. Rottgering et al., 1997; Ensslin et al., 1998; Giacintucci et al., 2008; van Weeren et al., 2010; Pearce et al., 2017; Hoang et al., 2018; Di Gennaro et al., 2018). This is also supported by the detection of strongly polarised emission at the relic position (e.g. van Weeren et al., 2010; Di Gennaro et al., 2021b), which suggests amplification and compression of magnetic fields. Nonetheless, the nature of the (re)acceleration mechanism is still unclear (e.g. Vazza & Brüggen, 2014). Standard Fermi type-I acceleration mechanisms (e.g. Drury, 1983; Ensslin et al., 1998; Brunetti & Jones, 2014) sometimes require an unrealistic shock efficiency to justify the relic radio brightness, due to the low Mach number of the shocks ($\mathcal{M} \lesssim 2$, e.g. Hoang et al., 2017; Di Gennaro et al., 2019; Botteon et al., 2020). Re-acceleration of pre-existing relativistic plasma at the shock has been therefore proposed (e.g. Markevitch et al., 2005; Bonafede et al., 2014; Kang et al., 2017; van Weeren et al., 2017a). Examples which can are considered to indicate on-going re-acceleration are still limited to a few cases (e.g. van Weeren et al., 2017a; Di Gennaro et al., 2018).

Most of the statistical studies of diffuse radio emission are limited to the local Universe (i.e. $z \sim 0.2$; e.g. Cassano et al., 2013; Kale et al., 2015; Cuciti et al., 2021b,a). A handful of clusters up to $z \sim 0.5$ hosting diffuse radio emission have been recently reported in Giovannini et al. (2020). At high redshifts ($z \geq 0.6$), only a few exceptional clusters have been studied so far (e.g. "El Gordo" at $z = 0.87$, Lindner et al. 2014, PLCK G147.3-16.6 at $z = 0.645$, van Weeren et al. 2014 and PSZ2 G099.86+58.45 at $z = 0.616$ Cassano et al. 2019). All these observations were firstly carried out at GHz frequencies, and eventually followed up at lower frequencies (i.e. $\sim$ 100 MHz) to investigate the spectral characteristic of the observed radio halos. This approach however misses a large fraction of (ultra-)steep spectrum halos, because radio halos with $\alpha < -1.5$ are hardly detected at GHz frequencies.

Recently, in Di Gennaro et al. (2021a) we have presented the first statistical study of a sample of distant ($z \geq 0.6$) galaxy clusters, selected from the second Planck Sunyaev-Zel'dovic (SZ) catalog (Planck Collaboration et al., 2016) and observed with the LOFAR Two-Metre Sky Survey (LoTSS; Shimwell et al., 2017, 2019). We observed that 9 out of 19 clusters host diffuse radio emission. The radio halos are located in dynamically disturbed clusters, based on available X-ray observations (Chandra and/or XMM-Newton). Assuming turbulent re-acceleration,from the radio luminosities we estimated magnetic field strengths similar to nearby ($z \sim 0.2$) systems, in the same mass range. According to the turbulent re-acceleration scenario, a large fraction of distant radio halos should have steep integrated spectral indices ($\alpha < -1.5$) due to the increasing synchrotron and Inverse Compton (IC) losses. We have followed up those clusters hosting diffuse radio emission in Di Gennaro et al. (2021a) with the upgraded Giant Metrewave Radio Telescope (uGMRT). This represents the first high-frequency follow up of halos detected at low frequencies. The observed sample is listed in Table 6.1.

Throughout the paper, we assume a standard ΛCDM cosmology, with $H_0 = 70$ km s^{-1} Mpc^{-1}, $\Omega_m = 0.3$ and $\Omega_\Lambda = 0.7$.

6.2. Observations and data Reduction

6.2.1. LOFAR

We use the same dataset presented in Di Gennaro et al. (2021a). The sample was observed together with LoTSS (Shimwell et al., 2017, 2019), which consists of the 8 hours of observation for each pointing (see Table 6.2). We performed standard LOFAR data reduction, which includes direction-independent and direction-dependent calibration and imaging of the full LOFAR field of view using `prefactor` (van Weeren et al., 2016; Williams et al., 2016; de Gasperin et al., 2019), `killMS` (Tasse, 2014; Smirnov

Table 6.1: Physical properties of the galaxy clusters.

Cluster name	z	RA_{J2000} [deg]	Dec_{J2000} [deg]	$M_{SZ,500}$ [10^{14} $M_\odot$]	kpc/″
PSZ2 G086.93+53.18	0.675	228.50446	+52.81074	5.4 ± 0.5	7.125
PSZ2 G089.39+69.36	0.680	208.43748	+43.48470	5.7 ± 0.7	7.148
PSZ2 G091.83+26.11	0.822	277.78430	+62.24770	7.4 ± 0.4	7.676
PSZ2 G099.86+58.45	0.616	213.6909	+54.78029	6.8 ± 0.5	6.845
PSZ2 G126.28+65.62	0.820	190.5975	+51.43944	5.0 ± 0.7	7.670
PSZ2 G141.77+14.19	0.830	70.27167	+68.22275	7.7 ± 0.9	7.700
PLCK G147.3–16.6	0.645	44.105898	+40.290140	6.3 ± 0.4	6.988
PSZ2 G147.88+53.24	0.600	164.37923	+57.99591	6.5 ± 0.6	6.762
PSZ2 G160.83+81.66	0.888	186.74267	+33.54682	$5.7^{+0.6}_{-0.7}$	7.865

The cluster masses, $M_{SZ,500}$, are taken from the Planck-SZ catalog (Planck Collaboration et al., 2016).

Table 6.2: Radio observation details.

Cluster name	Telescope	Project	Observation date [dd-mm-yyyy]	Observation length† [h]	Frequency coverage [MHz]	Configuration
PSZ2 G086.93+53.18	LOFAR	P227+53	19-02-2015	8.33	120–168	HBA Dual Inner
		P231+53	19-02-2015			
	uGRMT	38_054	30-08-2020	6	550–900	Band 4
PSZ2 G089.39+69.36	LOFAR	P207+45	07-05-2015	8.33	120–168	HBA Dual Inner
		P209+42	05-03-2015			
	uGMRT	38_054	25-08-2020	6	250–500	Band 3
PSZ2 G091.83+26.11	LOFAR	P275+63	22-08-2016	8.33	120–168	HBA Dual Inner
		P280+60	18-01-2019			
	uGMRT	36_039	05-05-2019	5	250–500	Band 3
	uGRMT	36_039	29-05-2019	5	550–900	Band 4
PSZ2 G099.86+58.45	LOFAR	P209+55	30-04-2015	8.33	120–168	HBA Dual Inner
		P214+52	12-05-2015			
		P214+55	12-05-2015			
	uGRMT	38_054	30-08-2020	6	550–900	Band 4
PSZ21 G126.28+65.62	LOFAR	P29Hetdex19	26-06-2014	8.33	120–168	HBA Dual Inner
		P30Hetdex06	30-05-2014			
		P33Hetdex08	19-06-2014			
	uGRMT	38_054	10-07-2020	6	550–900	Band 4
PSZ2 G141.77+14.19	LOFAR	P068+69	08-09-2017	8.33	120–168	HBA Dual Inner
	uGRMT	36_039	07-05-2019	5	550–900	Band 4
PLCK G147.3–16.6	LOFAR	P044+39	29-11-2017	8.33	120–168	HBA Dual Inner
	uGRMT	38_054	20-06-2020	6	550–900	Band 3
	uGRMT	38_054	16-06-2020	6	550–900	Band 4
PSZ2 G147.88+53.24	LOFAR	P165+57	11-05-2015	8.33	120–168	HBA Dual Inner
		P166+60	13-10-2017			
	uGRMT	38_054	20-06-2020	6	550–900	Band 4
PSZ2 G160.83+81.66	LOFAR	P185+32	11-12-2019	8.33	120–168	HBA Dual Inner
		P185+35	23-02-2017			
		P188+32	18-08-2017			
		P188+35	28-03-2019			
	uGRMT	38_054	12-08-2020	6	550–900	Band 4

†The observation length includes also the time on the calibrators.

& Tasse, 2015) and DDFacet (Tasse et al., 2018, 2021). Additionally, we performed extra phase and amplitude self-calibration loops to improve the quality of the calibration, using the products of the pipeline[1] and subtracting all of the sources outside of a region of $15' \times 15'$ surrounding the target (van Weeren et al., 2020). Final imaging was done with WSClean (Offringa et al., 2014; Offringa & Smirnov, 2017) with the wideband deconvolution mode (channelsout=6). The images have a central frequency of 144 MHz. The systematic uncertainty due to residual amplitude errors is set to 15% (Shimwell et al., 2019).

6.2.2. uGMRT

The clusters presented in this work have been observed with the uGMRT in Band 3 (250–550 MHz) and/or Band 4 (550–900 MHz). The total length of the observation is 6 hours, except for PSZ2 G091.83+26.11 and PSZ2 G141.77+14.19 which have been observed for 5 hours (see Table 6.2). Data were recorded in 2048 frequency channels with an integration time of 4 s in full Stokes mode. We used 3C286, 3C147 and 3C48 as primary calibrators, depending on the target. To process the data, we run the Source Peeling and Atmospheric Modeling (SPAM, Intema et al., 2009) on 6 sub-bands, of 33.3 MHz bandwidth each for the Band 3, and on 4 sub-bands, of 50.0 MHz bandwidth each for the Band 4. For each Band, the sub-bands are then imaged together using WSClean, at the common frequency of 400 and 650 MHz, for Band 3 and 4 respectively. The systematic uncertainties due to residual amplitude errors are set to 8% and 5%, for the observations in Band 3 and 4 respectively (Chandra et al., 2004).

6.3. Results

6.3.1. Images and integrated flux densities

For all clusters, we produced the final deep images using WSClean, with weighting= 'Briggs' and robust=-0.5. Only for the LOFAR images, we applied an inner uv-cut of 80λ (van Weeren et al., 2020). The final noise levels range between $\sim 50-150$ μJy beam^{-1}, $\sim 20-60$ μJy beam^{-1} and $\sim 7-12$ μJy beam^{-1} for the 144, 400 and 650 MHz full-resolution images, respectively (see Tab. 6.3). This means that the 650 MHz observations are about three times deeper than the LOFAR ones for the compact sources detection, i.e. assuming a typical spectral index $\alpha = -0.8$. For steep-spectra sources, i.e. $\alpha = -1.5$ the sensitivities of the two arrays are similar. The low resolution images, for both the LOFAR and uGMRT observations, were produced by applying a Gaussian taper at different resolutions to down weight the visibilities from longer baselines. We display all the images in

[1] https://github.com/mhardcastle/ddf-pipeline

Table 6.3: Imaging parameters and image properties of the cluster sample.

Cluster name	Central Frequency [MHz]	Resolution [$'' \times ''$]	uv min [λ]	uv-taper [$''$]	$\sigma_{\rm rms}$ [μJy beam^{-1}]
PSZ2 G086.93+53.18	144	9.5 × 4.5	80	–	91.8
		26.0 × 26.0	80	15	239.4
	650	3.8 × 3.4	–	–	8.6
		26.0 × 26.0	–	15	45.5
PSZ2 G089.39+69.36	144	8.3 × 4.8	80	–	64.3
		29.0 × 29.0	80	15	138.2
	400	6.4 × 5.1	–	–	57.2
		29.0 × 29.0	–	15	47.0
PSZ2 G091.83+26.11	144	6.8 × 4.5	80	–	92.1
		14.0 × 14.0	160	6	188.4
	400	13.8 × 6.2	–	–	64.6
		14.0 × 14.0	160	–	94.6
	650	4.4 × 2.8	–	–	11.4
		14.0 × 14.0	160	6	38.9
PSZ2 G099.86+58.45	144	8.0 × 4.4	80	–	66.3
		18.0 × 18.0	180	10	153.2
	650	5.0 × 2.6	–	–	8.2
		18.0 × 18.0	180	10	33.7
PSZ2 G126.28+65.62	144	7.6 × 4.5	80	–	52.3
		25.0 × 25.0	80	15	117.6
	650	7.6 × 2.5	–	–	9.8
		25.0 × 25.0	–	15	39.9
PSZ2 G141.77+14.19	144	7.6 × 5.0	80	–	119.6
		17.0 × 17.0	150	10	171.0
	650	6.4 × 3.3	–	–	9.7
		17.0 × 17.0	150	10	21.3
PLCK G147.3–16.6	144	7.6 × 5.9	80	–	152.8
		17.0 × 17.0	150	10	315.6
	400	8.0 × 4.1	–	–	22.3
		17.0 × 17.0	150	10	58.1
	650	3.4 × 3.0	–	–	7.3
		17.0 × 17.0	150	10	25.5
PSZ2 G147.88+53.24	144	8.6 × 4.6	80	–	61.7
		14.0 × 14.0	100	6	123.4
	650	5.6 × 2.6	–	–	8.5
		14.0 × 14.0	100	6	19.5
PSZ2 G160.83+81.66	144	13.1 × 4.6	80	–	138.2
		22.0 × 22.0	80	10	221.3
	650	4.5 × 2.6	–	–	9.2
		22.0 × 22.0	–	10	22.7

Figures 6.1 to 6.9. Among the nine clusters presented in this work, five of them show extended diffuse radio emission in the uGMRT observations.

To obtain the flux densities of the radio halos, we produced source-subtracted images. We applied a uv-cut to the data, to filter out emission associated with sources of linear sizes larger than 500 kpc at the cluster redshift, and to create a clean component model of the compact sources. Given the smaller sizes of the halo, for the LOFAR image of PSZ2 G089.39+69.36 we employed an inner uv-cut of 400 kpc. During this step, we employed multiscale deconvolution using scales of $[0, 4, 8, 16] \times$ pixelscale (with the pixel size of $1.5''$, $2''$ and $1''$ for the 144, 400 and 650 MHz images, respectively) to include and subtract the diffuse emission from the radio galaxies. For the automatic deconvolution, we used a mask threshold of $1\sigma_{\rm rms}$ to subtract the faintest contaminating sources. Finally, we subtracted the compact source models from the visibilities, and tapered the uv-data with different Gaussian tapers (i.e. $6''$ and $10''$). For an extended radio galaxy with a linear size $\gtrsim 500$ kpc, we cannot properly subtract the radio emission from the uv-data (Di Gennaro et al., 2021a). This is the case for the candidate radio relic in PSZ2 G091.83+26.11 and for the radio galaxy northward of PLCK G147.3–16.6, which have been manually excluded from the radio halo region.

We measure the radio halo flux densities for each cluster from the same regions, in the LOFAR and uGMRT images, encompassing the full extent of the diffuse radio emission. Uncertainties on the halo flux densities are obtained by taking into account the systematic uncertainties due to residual amplitude errors (f), the map noise level and the uncertainty of the source subtraction in the uv plane ($\sigma_{\rm sub}$, i.e. few percent of the residual flux from compact sources):

$$\Delta S_\nu = \sqrt{(f S_\nu)^2 + N_{\rm beam}\sigma_{\rm rms}^2 + \sigma_{\rm sub}^2} \, . \tag{6.1}$$

In those systems with no detection of diffuse emission in the uGMRT images, we derived upper limits as $\sigma_{\rm rms}\sqrt{N_{\rm beam}}$, with $N_{\rm beam}$ the number of beams covering the halo region and $\sigma_{\rm rms}$ the map noise level. The resulting flux densities, both measured and upper limits, are listed in Table 6.4.

6.3.2. Spectral index maps and integrated spectral indices

To produce the spectral index maps of those clusters with diffuse radio emission in both LOFAR and uGMRT observations, we made images with a common inner uv-cut to compensate for the different interferometer uv-coverage. To emphasise the presence of the radio halo, we also applied a Gaussian taper. The images were then convolved to the same resolution, and re-gridded to the same pixel grid (i.e. the LOFAR image). The effective final resolutions and the noise levels of each image are listed in Table

6.3. For the clusters with observations at three frequencies, we used the same procedure used in Di Gennaro et al. (2018), where a second-order polynomial fit was used in the case of significant curvature (i.e. above the 2σ threshold, where σ is the uncertainty associated with the second-order term). In this case, the spectral index was calculated at 400 MHz, i.e. the median of the total band. We blanked all the pixels below the $2\sigma_{\rm rms}$ threshold for each frequency, with $\sigma_{\rm rms}$ the noise level reported in Table 6.3. The spectral index uncertainty maps are obtained via 150 Monte Carlo simulations of the first-/second-order polynomial fit. We assumed that the uncertainty of each flux given by the sum in quadrature of the noise map and the systematic flux uncertainties, i.e. $\sqrt{(fS_\nu)^2 + \sigma_{\rm rms}^2}$. For the clusters with observations at only two frequencies, we calculate the spectral index analytically, with an uncertainty of:

$$\Delta\alpha = \frac{1}{\ln\frac{\nu_1}{\nu_2}}\sqrt{\left(\frac{\Delta S_1}{S_1}\right)^2 + \left(\frac{\Delta S_2}{S_2}\right)^2}\,. \tag{6.2}$$

For the clusters hosting no diffuse radio emission in the uGMRT observations, we derived upper limits on the integrated spectral indices, according to

$$\alpha = \log\left(\frac{S_{144} - \Delta S_{144}}{S_{\rm uGMRT}}\right)/\log\left(\frac{144\ {\rm MHz}}{\nu_{\rm uGMRT}}\right)\,, \tag{6.3}$$

where the subscript ‘uGMRT’ refers to the Band 4 or 3.

6.3.3. Individual clusters

In this subsection we provide a brief description of each cluster, at the three observing frequencies.

PSZ2 G086.93+53.18

This is the faintest radio halo detected in the LOFAR observations ($S_{144} = 5.6 \pm 1.1$ mJy), with a largest linear size LLS$_{144} = 0.4 - 0.5$ Mpc. No diffuse radio emission is visible at 650 MHz, despite the better depth of the observation (see Fig. 6.1). From the same halo region, we derive an upper limit for the flux of $S_{650} < 0.5$ mJy, corresponding to an upper limit on the spectral index of $\alpha < -1.5$.

PSZ2 G089.39+69.36

A Mpc-scale radio halo is found in the LOFAR observations ($S_{144} = 10.0 \pm 1.6$ mJy, LLS$_{144} = 1$ Mpc). No diffuse radio emission is observed in the 400 MHz image (Fig. 6.2). We derive an upper limit for the flux of $S_{400} < 1.2$ mJy, corresponding to an upper limit on the spectral index of $\alpha < -1.9$.

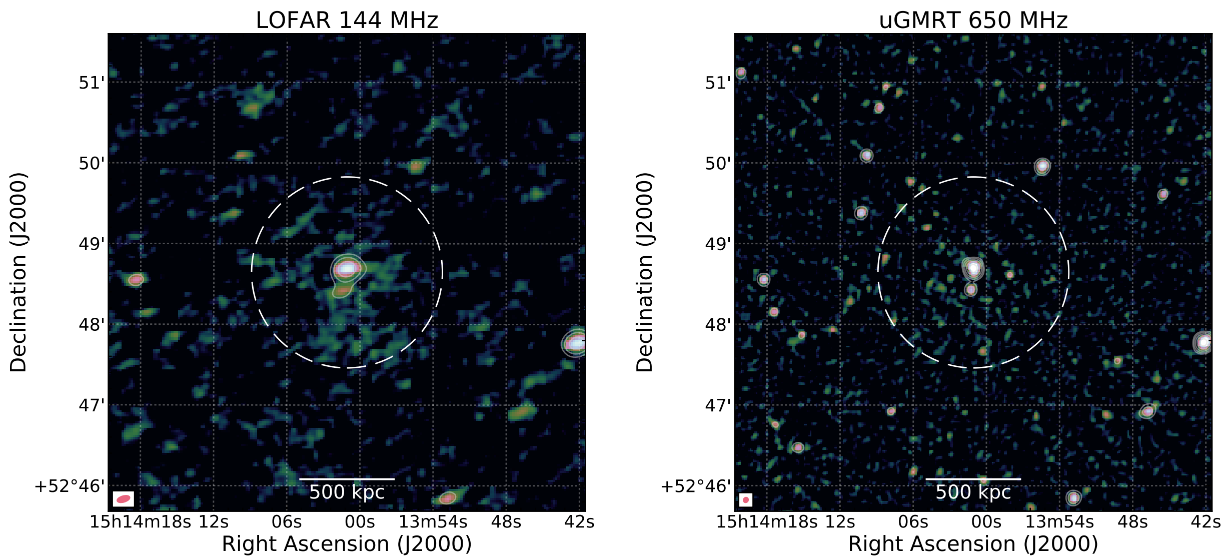

Figure 6.1: PSZ2 G086.93+53.18. Full-resolution images (`weighting='Briggs'` and `robust=-0.5`) at 144 MHz (left) and 650 MHz (right). White-coloured radio contours are drawn at levels of $2.5\sigma_{\rm rms} \times [-1, 1, 2, 4, 8, 16, 32]$, with $\sigma_{\rm rms}$ the noise level at each frequency (see Table 6.3. The negative contour level is drawn with a dashed white line. The dashed white circle in each map shows the $R = 0.5R_{\rm SZ,500}$ region, obtained from $M_{\rm SZ,500}$.

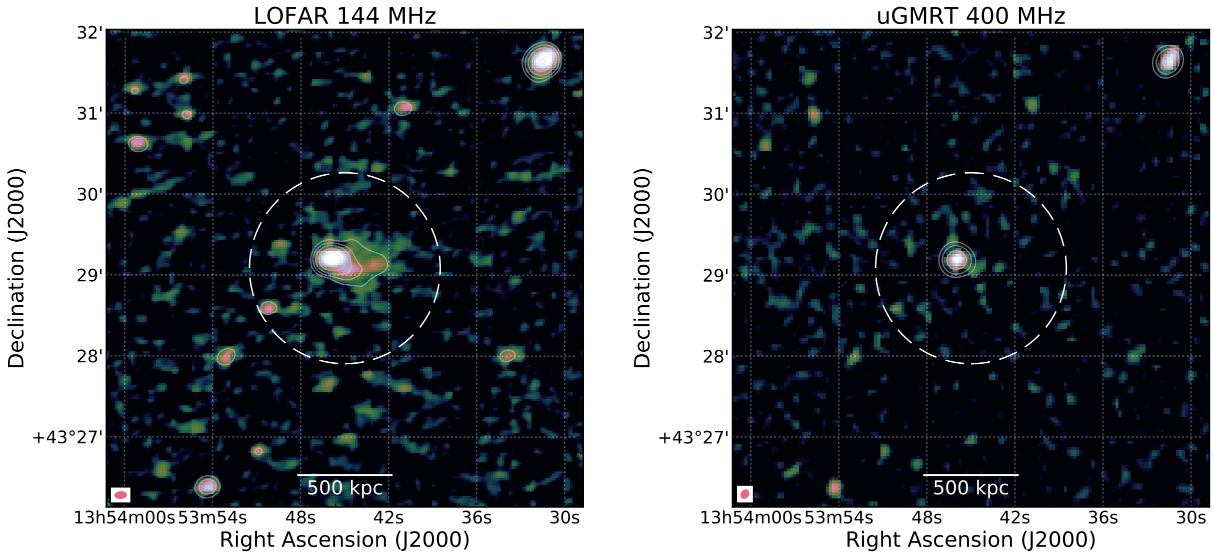

Figure 6.2: PSZ2 G089.39+69.36. Full-resolution images (`weighting='Briggs'` and `robust=-0.5`) at 144 MHz (left) and 400 MHz (right). White-coloured radio contours are drawn at levels of $2.5\sigma_{\rm rms} \times [-1, 1, 2, 4, 8, 16, 32]$, with $\sigma_{\rm rms}$ the noise level at each frequency (see Table 6.3. The negative contour level is drawn with a dashed white line. The dashed white circle in each map shows the $R = 0.5R_{\rm SZ,500}$ region, obtained from $M_{\rm SZ,500}$.

PSZ2 G091.83+26.11

The radio halo in this cluster is the brightest in our sample, at all three frequencies (see Fig. 6.3). The largest linear size of the radio halos is the same in both the LOFAR and uGMRT observations, i.e. about 1.2 Mpc. The 650 MHz observation is the deepest of the three frequencies, where we also see some substructures in the halo. We measure a flux density of S_{144} = 65.4 ± 9.9 mJy, S_{400} = 23.9 ± 2.0 mJy and S_{650} = 14.5 ± 0.8 mJy for the LOFAR, uGMRT Band 3 and uGMRT Band 4 observations. These correspond to integrated spectral indices of $\alpha_{650}^{144} = -1.00 \pm 0.11$, $\alpha_{400}^{144} = -0.99 \pm 0.17$ and $\alpha_{650}^{400} = -1.03 \pm 0.21$. These values are consistent with a single power-law spectral shape. The spectral index map shows a somewhat steeper spectral index in the central part of the cluster, with α_{400} between ~ -1.2 and ~ -1.4. Northward, the spectral index flattens, with $\alpha_{650}^{144} \sim -0.75$, in correspondence of sources C and D.

In the east and southeast direction, the elongated source that was classified as a candidate radio relic in Di Gennaro et al. (2021a) maintains its morphology. This source can be divided into two pieces. One (R1), located east the cluster centre, is a faint patchy filament that is 80″ long and 8″ wide, corresponding to 640×60 kpc^2 at the cluster redshift. The other (R2), located southeastward, is brighter and extends for about 40″ (i.e. 300 kpc at the cluster redshift). Interestingly, its morphology resembles a double-lobe radio galaxy at 650 MHz. However, no optical counterpart is visible from the available PanSTARRS (Panoramic Survey Telescope and Rapid Response System; Chambers et al., 2016) optical image (see Appendix .1). However, we note that the optical image is rather shallow, and might miss faint galaxies. Possibly, R2 combines the emission of a radio relic and a double-lobe radio galaxy. Observations with the Karl-Jansky Very Large Telescope (VLA) in the 1–4 GHz band will help in the classification of this elongated piece of emission. In particular, the polarisation characteristics will be crucial and will be presented in forthcoming work (Di Gennaro et al., in prep). We measure the flux density for the candidate radio relic from the low-resolution images (i.e. $14'' \times 14''$), considering the full length of the source (i.e. R1+R2). Since at this resolution the compact sources B, C and D are embedded in the candidate relic, we measured their flux densities from the full-resolution image and we subtracted them arithmetically from the total flux density. We obtain S_{144} = 274.8 ± 45.6 mJy, S_{400} = 76.6 ± 6.5 mJy and S_{650} = 36.3 ± 2.1 mJy, corresponding to $\alpha_{650}^{144} = -1.34 \pm 0.12$ ($\alpha_{400}^{144} = -1.25 \pm 0.18$ and $\alpha_{650}^{400} = -1.54 \pm 0.21$). The spectral index map shows hints of steepening for R2 (up to $\alpha_{400} \sim -2$), which is typical of radio relics (e.g. Di Gennaro et al., 2018; Rajpurohit et al., 2018b). This is not observed for R1. Next to the candidate relic, source B is characterised by a very steep spectrum ($\alpha_{400} \sim -2$).

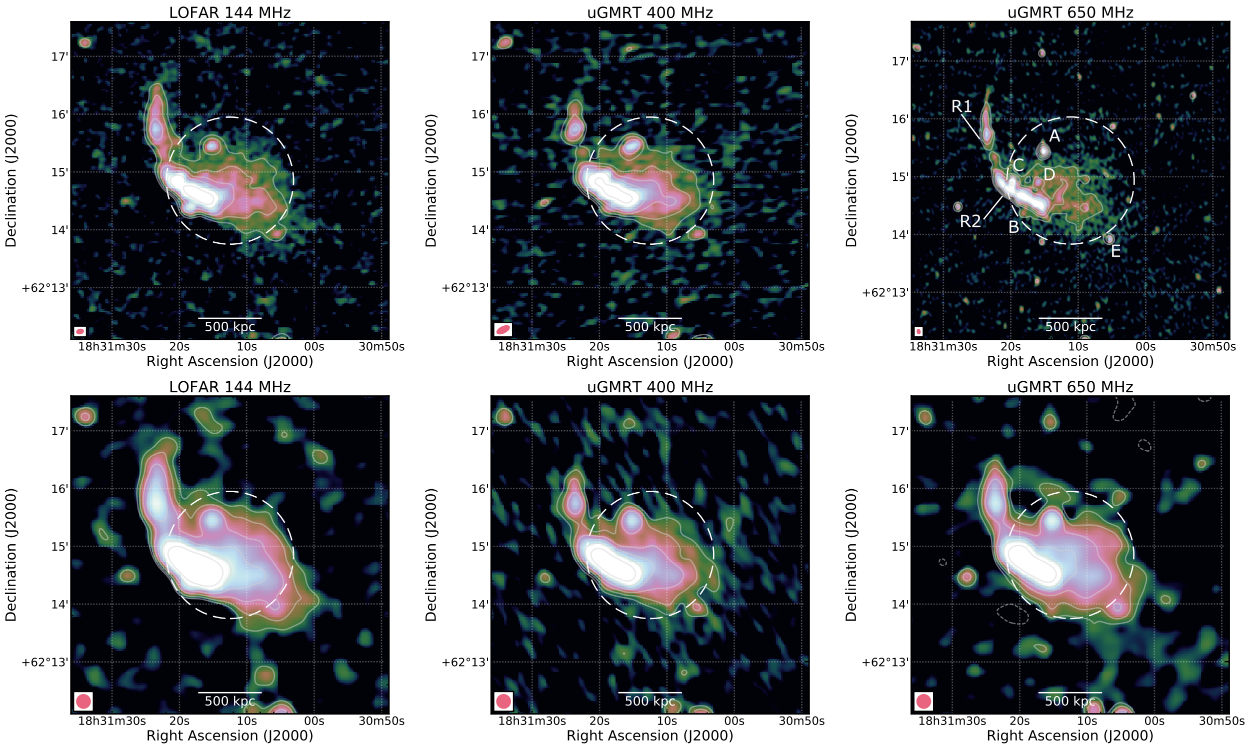

Figure 6.3: PSZ2 G091.83+26.11. Top and bottom rows: Full-resolution and 14″ images (`weighting='Briggs'` and `robust=-0.5`) at 144 MHz (left), 400 MHz (middle) and 650 MHz (right). White-coloured radio contours are drawn at levels of $2.5\sigma_{\rm rms} \times [-1, 1, 2, 4, 8, 16, 32]$, with $\sigma_{\rm rms}$ the noise level at each frequency (see Table 6.3. The negative contour level is drawn with a dashed white line. The dashed white circle in each map shows the $R = 0.5R_{\rm SZ,500}$ region, obtained from $M_{\rm SZ,500}$.

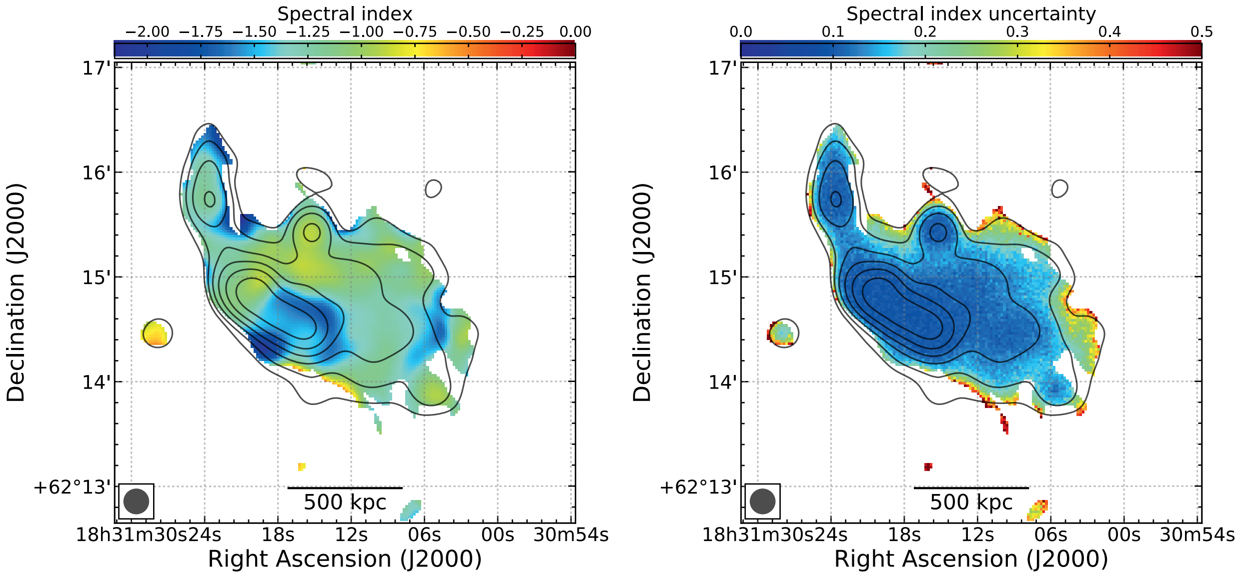

Figure 6.3: Continued. Spectral index map between 144, 400 and 650 MHz at 14″ resolution, and correspondent uncertainty map (left and right panels, respectively). uGMRT radio contours at 650 MHz are drawn in black, at the levels $3\sigma_{\rm rms} \times [-1, 1, 2, 4, 8, 16, 32]$, with $\sigma_{\rm rms}$ the noise level (see Table 6.3).

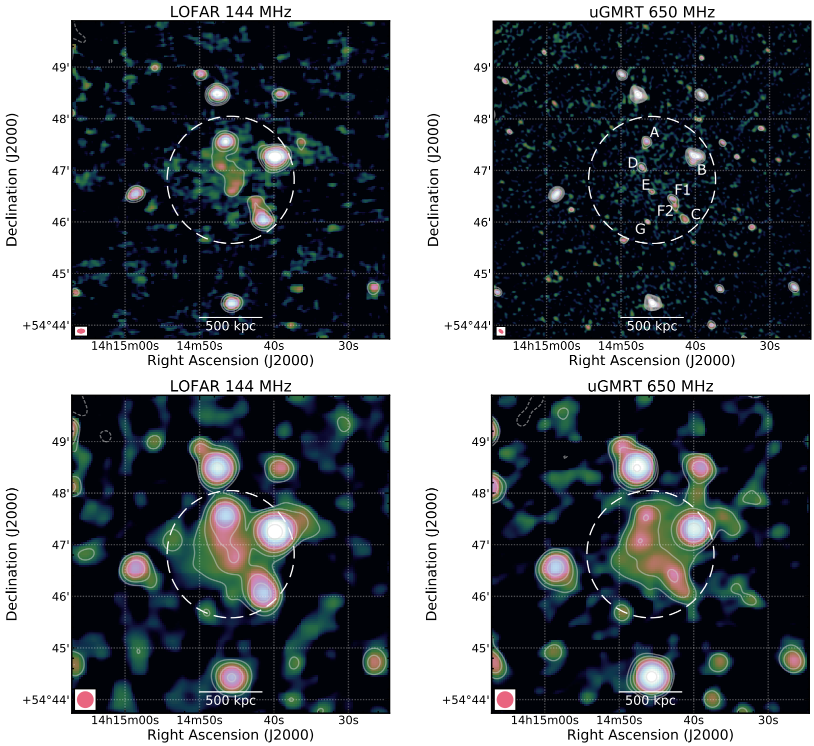

Figure 6.4: PSZ2 G099.86+58.45. Top and bottom rows: Full-resolution and 18″ images (`weighting='Briggs'` and `robust=-0.5`) at 144 MHz (left) and 650 MHz (right). White-coloured radio contours are drawn at levels of $2.5\sigma_{\rm rms}\times[-1, 1, 2, 4, 8, 16, 32]$, with $\sigma_{\rm rms}$ the noise level at each frequency (see Table 6.3). The negative contour level is drawn with a dashed white line. We followed Cassano et al. (2019) for the source labelling (their source 1, 2 and 3 became D, E and F1+F2, respectively). The dashed white circle in each map shows the $R = 0.5R_{\rm SZ,500}$ region, obtained from $M_{\rm SZ,500}$.

PSZ2 G099.86+58.45

We detect diffuse radio emission in the 650 MHz observations, similar to what is visible at 144 MHz (Fig. 6.4, LLS_{144} = 1.2 and LLS_{650} = 0.95 Mpc). We measure a flux density of $S_{144} = 18.1\pm2.9$ mJy and $S_{650} = 4.0\pm0.4$ mJy for the LOFAR and uGMRT Band 4 observations. This corresponds to an integrated spectral index of $\alpha_{650}^{144} = -1.00 \pm 0.13$. The spectral index map in Fig. 6.4 shows steeper values at the cluster centre (i.e. $\alpha_{650}^{144} \sim -1.6$) and flatter at the cluster outskirts (i.e. $\alpha_{650}^{144} \sim -0.9$) For this cluster, also L-band VLA observations are available (Cassano et al., 2019). In these observations, hints of a halo are present only at the $2\sigma_{\rm rms}$ level (with

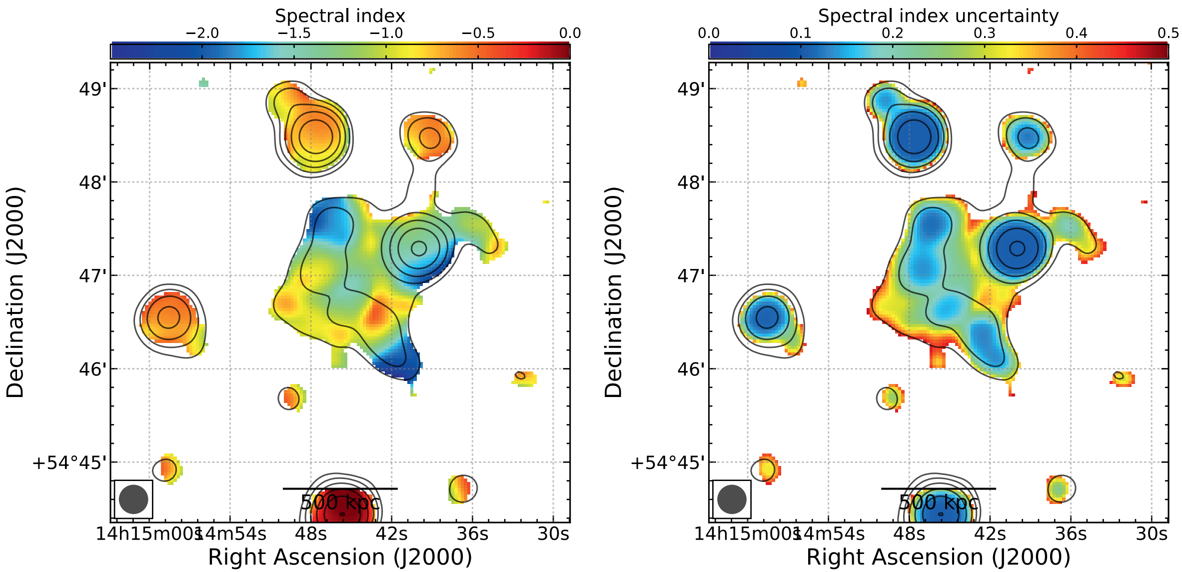

Figure 6.4: Continued. Spectral index map between 144 and 650 MHz at 18″ resolution, and correspondent uncertainty map (left and right panels, respectively). uGMRT radio contours at 650 MHz are drawn in black, at the levels $3\sigma_{\rm rms} \times [-1, 1, 2, 4, 8, 16, 32]$, with $\sigma_{\rm rms}$ the noise level (see Table 6.3).

$\sigma_{\rm rms,VLA}$ = 20 μJy beam^{-1}). We repeated the flux measurement, covering the same region of the LOFAR halo, finding a flux of $S_{1500} \sim 1.0 \pm 0.4$ mJy, in agreement with the flux density reported in Cassano et al. (2019). This VLA flux density suggests a mild steepening towards GHz frequencies, with $\alpha_{1500}^{650} \sim -1.7 \pm 0.5$.

As for PSZ2 G091.83+26.11, also in this cluster we detect ultra-steep spectra from source A ($\alpha_{600}^{144} \sim -1.7$) and source C ($\alpha_{650}^{144} \sim -2.5$), as was also mentioned by Cassano et al. (2019).

PSZ2 G126.28+65.62

No diffuse radio emission is found in the uGMRT 650 MHz observations (see right panel Fig. 6.5, LLS$_{144}$ = 0.8 Mpc). We measure $S_{144} = 6.8 \pm 1.1$ mJy and derive an upper limit of $S_{650} < 0.5$ mJy for the radio halos, corresponding to an upper limit on the spectral index of $\alpha < -1.6$.

PSZ2 G141.77+14.19

Hints of the presence of diffuse emission are present in the uGMRT 650 MHz data, around sources D, E, F and G (see right panel Fig. 6.6, LLS$_{144}$ = 0.6 and LLS$_{650}$ = 0.55 Mpc). We measure a flux density of S_{144} = 6.5 ± 1.2 mJy and $S_{650} = 1.2 \pm 0.1$ mJy from the same halo region. This corresponds to a spectral index of $\alpha_{650}^{144} = -1.12 \pm 0.13$, and it agrees with the values found in the spectral index map.

PLCK G147.3–16.6

Observations at 610 MHz with the GMRT were published by van Weeren et al. (2014), where a radio halo was discovered. With the new wide-band GMRT observations we confirm the presence of a Mpc-size radio halo at both 400 and 650 MHz (Fig. 6.7). Interestingly, in the two uGMRT observations, the diffuse emission appears to be larger than the LOFAR image (LLS$_{144}$ = 0.8, LLS$_{400}$ = 1 and LLS$_{650}$ = 1 Mpc). However, we note that this observation is less deep, probably due to a bad ionosphere. The flux densities encompassed in the area covered by the halo in the LOFAR images are $S_{144} = 21.0 \pm 3.7$ mJy, $S_{400} = 5.4 \pm 0.6$ mJy and $S_{650} = 2.8 \pm 0.3$ mJy for the 144 MHz, 400 MHz and 650 MHz observations. Increasing the region to cover the full extension of the halo in in the uGMRT images, we obtain $S_{144} = 26.6 \pm 4.4$ mJy, $S_{400} = 10.0 \pm 0.9$ mJy and $S_{650} = 5.6 \pm 0.4$ mJy. We note that the 650 MHz flux we report is slightly below the one found by van Weeren et al. (2014). This is probably due to a better subtraction of the contribution of the compact sources with the deeper wide-band observations. Given the integrated flux densities, we obtain spectral indices of $\alpha_{650}^{144} = -1.34 \pm 0.15$, $\alpha_{400}^{144} = -1.33 \pm 0.20$ and $\alpha_{650}^{400} = -1.35 \pm 0.37$, in the small area, and $\alpha_{650}^{144} = -1.03 \pm 0.12$, $\alpha_{400}^{144} = -0.96 \pm 0.19$ and $\alpha_{650}^{400} = -1.19 \pm 0.23$,

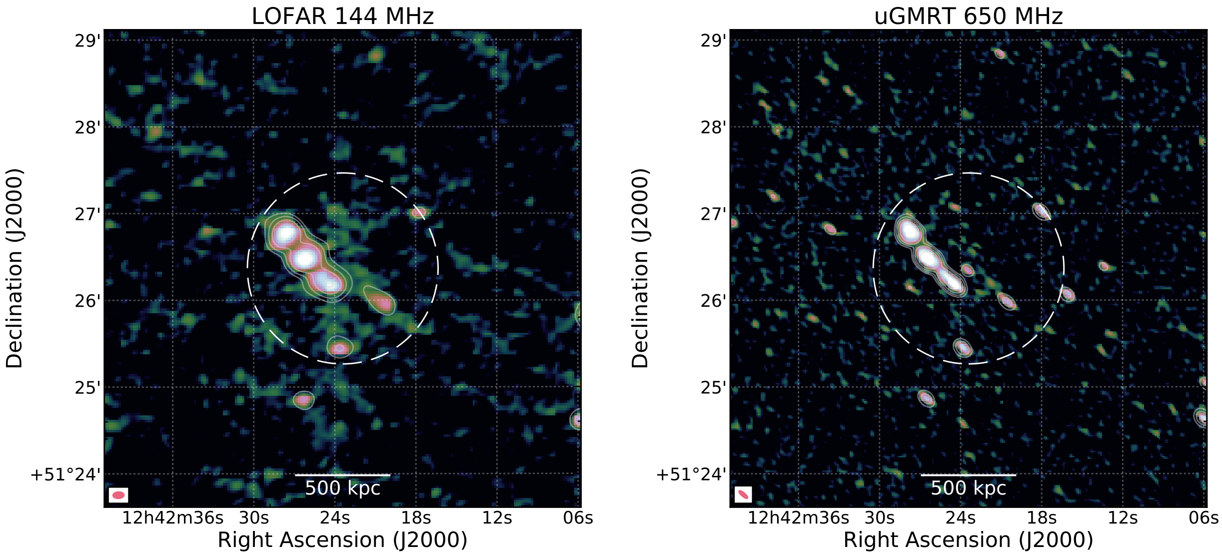

Figure 6.5: PSZ2 G126.28+65.62. Full-resolution images (`weighting='Briggs'` and `robust=-0.5`) at 144 MHz (left) and 650 MHz (right). White-coloured radio contours are drawn at levels of $2.5\sigma_{\rm rms} \times [-1, 1, 2, 4, 8, 16, 32]$, with $\sigma_{\rm rms}$ the noise level at each frequency (see Table 6.3. The negative contour level is drawn with a dashed white line. The dashed white circle in each map shows the $R = 0.5R_{\rm SZ,500}$ region, obtained from $M_{\rm SZ,500}$.

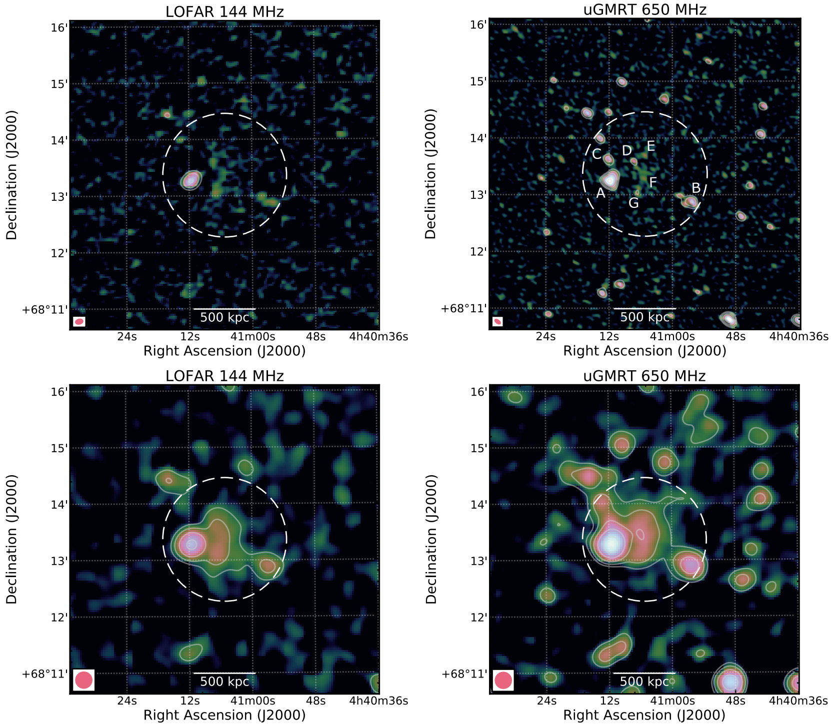

Figure 6.6: PSZ2 G141.77+14.19 . Top and bottom rows: Full-resolution and 17″ images (`weighting='Briggs'` and `robust=-0.5`) at 144 MHz (left) and 650 MHz (right). White-coloured radio contours are drawn at levels of $2.5\sigma_{\rm rms}\times[-1, 1, 2, 4, 8, 16, 32]$, with $\sigma_{\rm rms}$ the noise level at each frequency (see Table 6.3). The negative contour level is drawn with a dashed white line. The dashed white circle in each map shows the $R = 0.5R_{\rm SZ,500}$ region, obtained from $M_{\rm SZ,500}$.

in the big area. These values are consistent with a single power-law distribution. The spectral index map in Fig. 6.7 shows steeper spectral index in the halo centre, with $\alpha_{400} \sim -1.4$, in agreement with the integrated spectral indices in the small halo region.

PSZ2 G147.88+53.24

A Mpc-size diffuse radio emission at 144 MHz was reported in Di Gennaro et al. (2021a) ($\rm LLS_{144}$ = 0.6 Mpc). This is also confirmed by deep observations at the same frequency (Osinga et al., 2021). Hints of diffuse radio emission are visible in the 650 MHz image (see Fig. 6.8, $\rm LLS_{650}$ = 0.5 Mpc). Excluding sources D, E, F and G from the halo region, we measure $S_{144} = 8.2 \pm 1.3$ mJy and $S_{650} = 1.1 \pm 0.2$ mJy, for the LOFAR and uGMRT

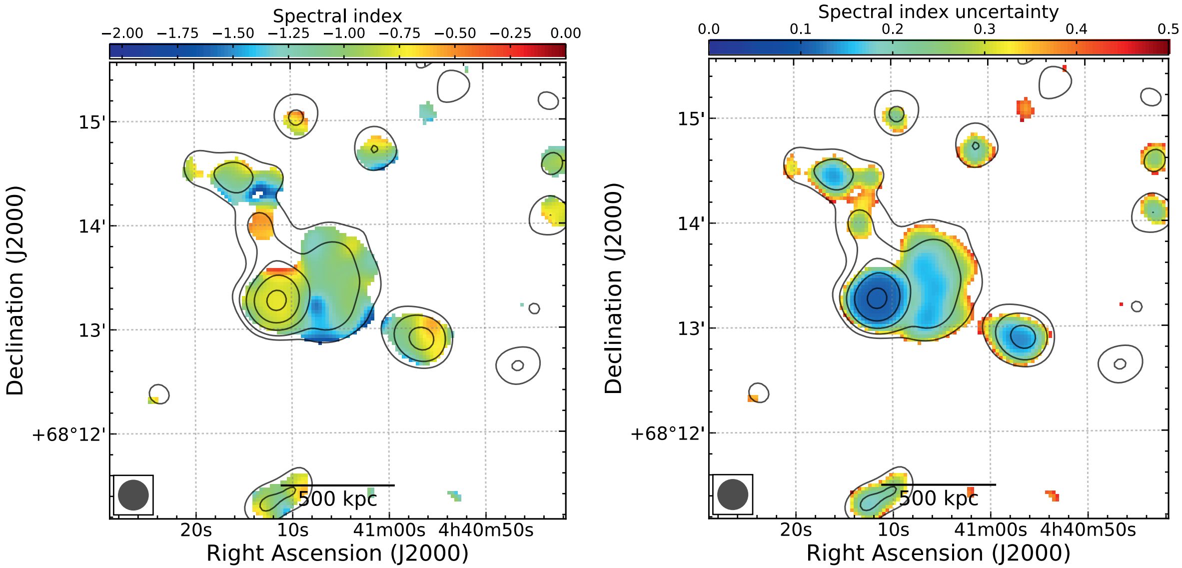

Figure 6.6: Continued. Spectral index map between 144 and 650 MHz at 17″ resolution, and correspondent uncertainty map (left and right panels, respectively). uGMRT radio contours at 650 MHz are drawn in black, at the levels $3\sigma_{\rm rms} \times [-1, 1, 2, 4, 8, 16, 32]$, with $\sigma_{\rm rms}$ the noise level (see Table 6.3).

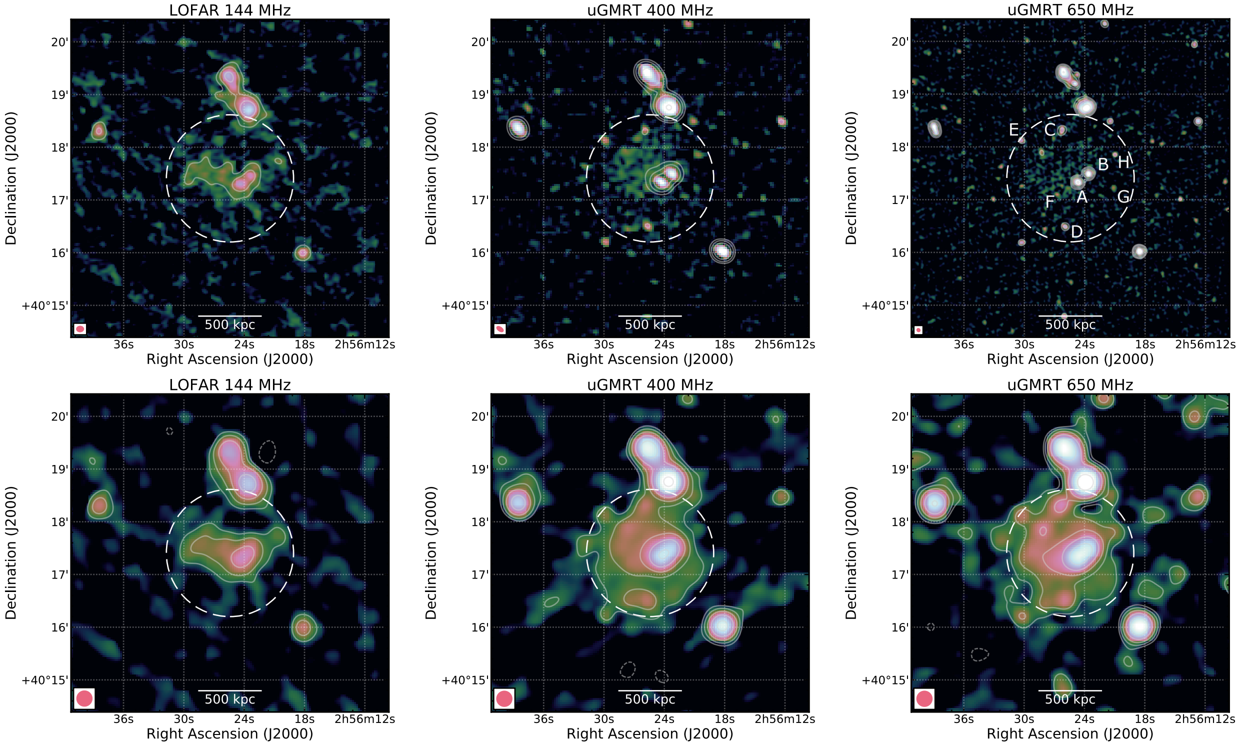

Figure 6.7: PLCK G147.3–16.6. Top and bottom rows: Full-resolution and 17″ images (`weighting=‘Briggs’` and `robust=-0.5`) at 144 MHz (left), 400 MHz (middle) and 650 MHz (right). White-coloured radio contours are drawn at levels of $2.5\sigma_{\rm rms} \times [-1, 1, 2, 4, 8, 16, 32]$, with $\sigma_{\rm rms}$ the noise level at each frequency (see Table 6.3). The negative contour level is drawn with a dashed white line. We followed van Weeren et al. (2014) for the source labelling. The dashed white circle in each map shows the $R = 0.5R_{\rm SZ,500}$ region, obtained from $M_{\rm SZ,500}$.

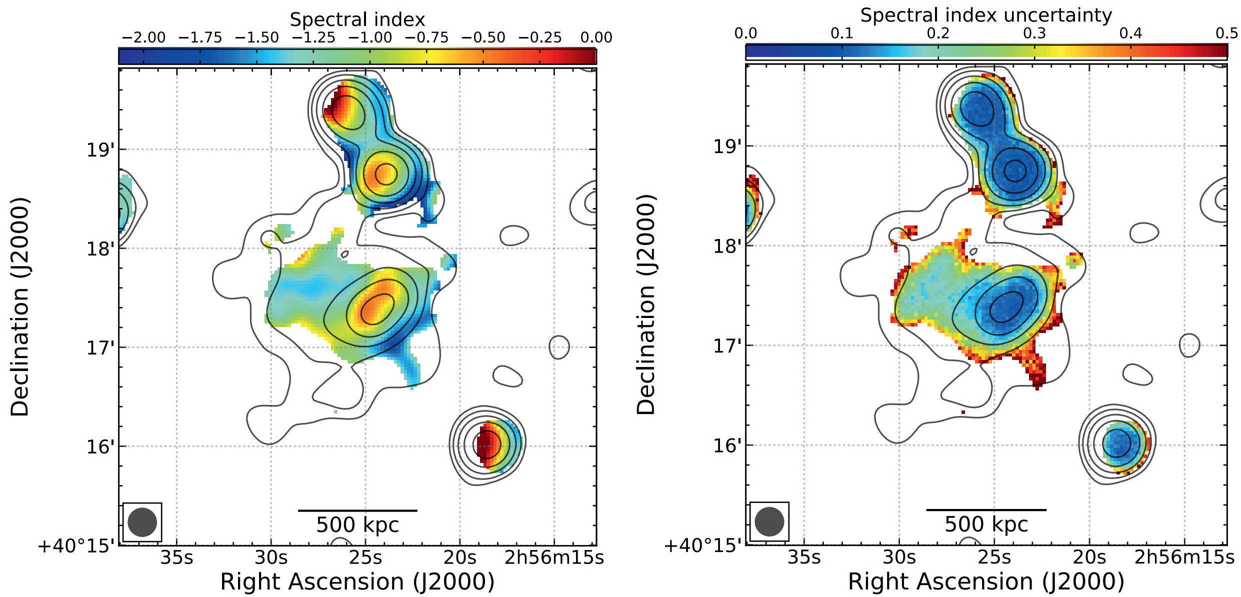

Figure 6.7: Continued. Spectral index map between 144, 400 and 650 MHz at 17″ resolution, and correspondent uncertainty map (left and right panels, respectively). uGMRT radio contours at 650 MHz are drawn in black, at the levels $3\sigma_{\rm rms} \times [-1, 1, 2, 4, 8, 16, 32]$, with $\sigma_{\rm rms}$ the noise level (see Table 6.3).

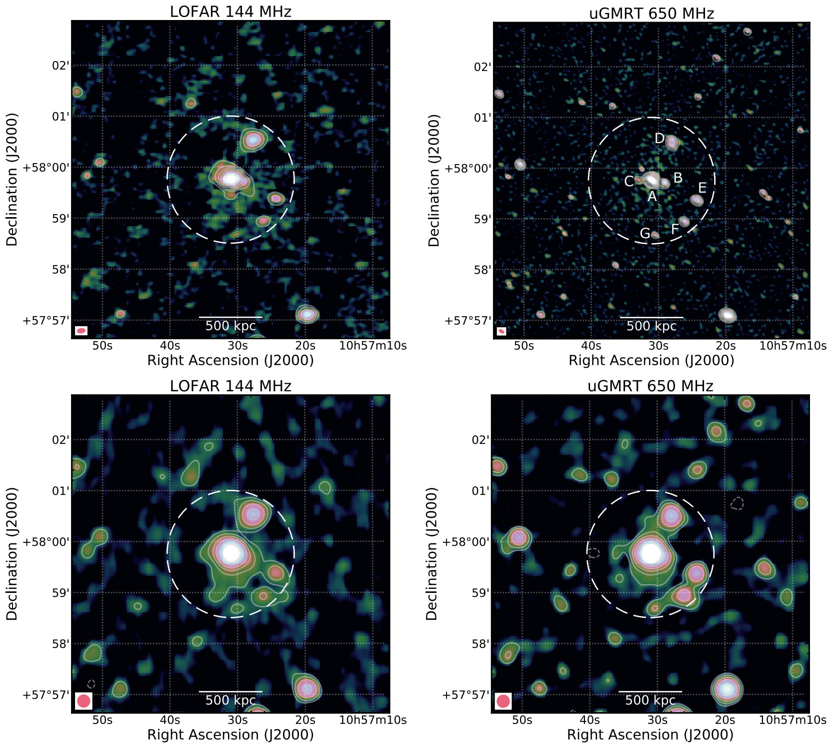

Figure 6.8: PSZ2 G147.88+53.24. Top and bottom rows: Full-resolution and 14″ images (`weighting='Briggs'` and `robust=-0.5`) at 144 MHz (right) and 650 MHz (left). White-coloured radio contours are drawn at levels of $2.5\sigma_{\rm rms}\times[-1, 1, 2, 4, 8, 16, 32]$, with $\sigma_{\rm rms}$ the noise level at each frequency (see Table 6.3). The negative contour level is drawn with a dashed white line. The dashed white circle in each map shows the $R = 0.5R_{\rm SZ,500}$ region, obtained from $M_{\rm SZ,500}$.

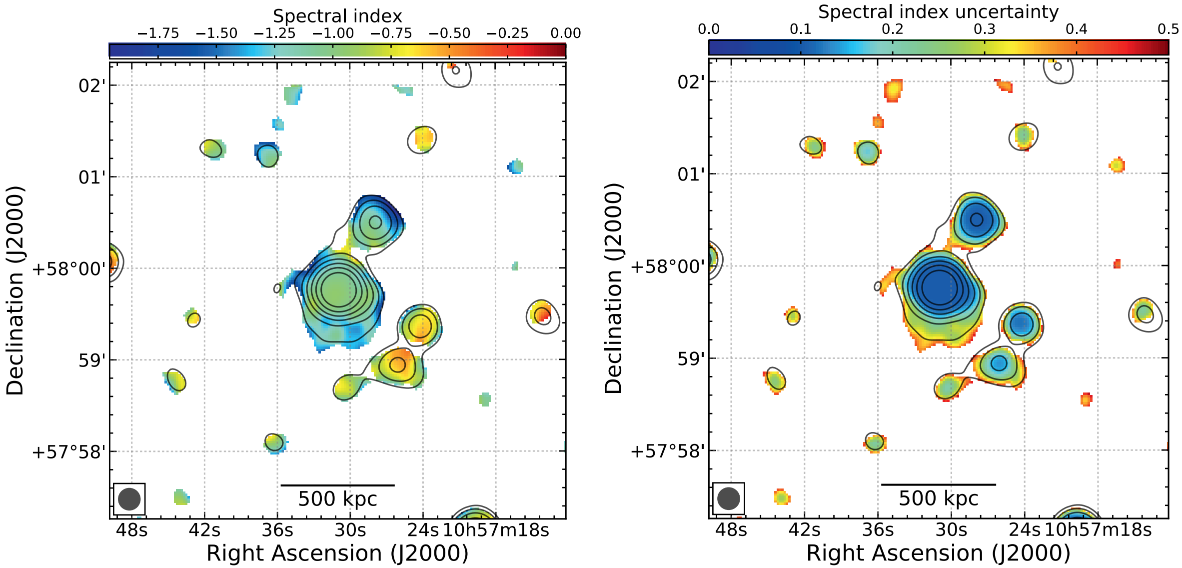

Figure 6.8: Continued. Spectral index map between 144 and 650 MHz at 14″ resolution, and correspondent uncertainty map (left and right panels, respectively). uGMRT radio contours at 650 MHz are drawn in black, at the levels $3\sigma_{\rm rms} \times [-1, 1, 2, 4, 8, 16, 32]$, with $\sigma_{\rm rms}$ the noise level (see Table 6.3).

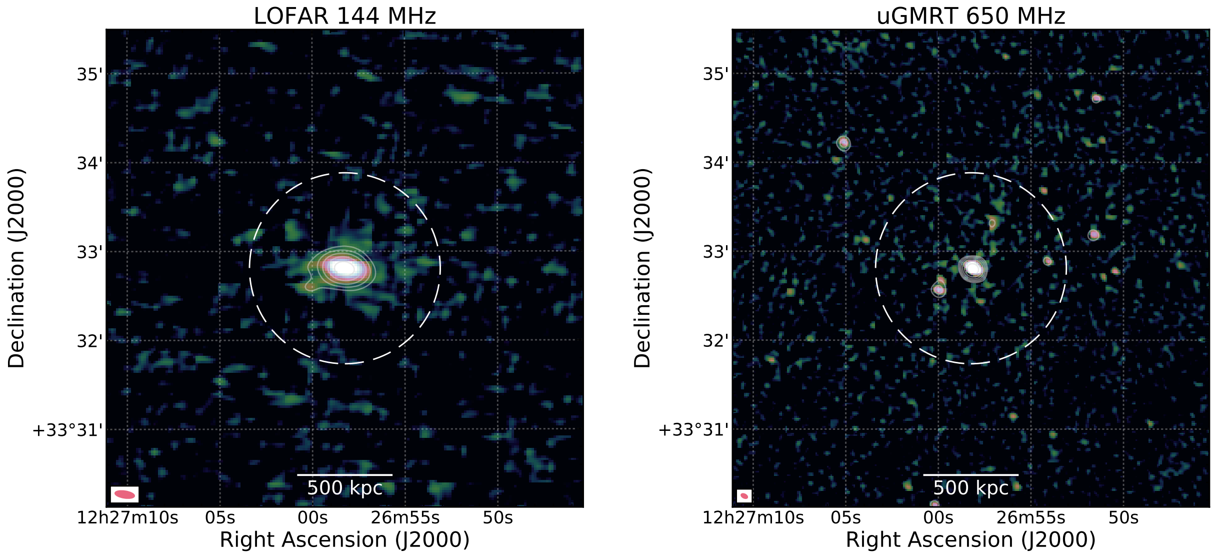

Figure 6.9: PSZ2 G160.83+81.66. Full-resolution images (`weighting='Briggs'` and `robust=-0.5`) at 144 MHz (left) and 650 MHz (right). White-coloured radio contours are drawn at levels of $2.5\sigma_{\rm rms} \times [-1, 1, 2, 4, 8, 16, 32]$, with $\sigma_{\rm rms}$ the noise level at each frequency (see Table 6.3. The negative contour level is drawn with a dashed white line. The dashed white circle in each map shows the $R = 0.5R_{\rm SZ,500}$ region, obtained from $M_{\rm SZ,500}$.

Band 4 observation respectively. This corresponds to a spectral index of $\alpha_{650}^{144} = -1.33 \pm 0.17$. The spectral index map for PSZ2 G147.88+53.24 is mostly dominated by the central compact source (i.e. source A, see Fig. 6.8), which is characterised by a spectral index $\alpha_{650}^{144} \sim -1$. Just south of it, we detect steeper spectral index values ($\alpha_{650}^{144} \sim -1.2$) that can be associated with the radio halo.

PSZ2 G160.83+81.66

This cluster represents the most distant radio halo found so far, at a redshift of 0.888 (S_{144} = 8.5 ± 1.5 mJy, LLS_{144} = 0.7 Mpc). No diffuse radio emission is visible at 650 MHz, where we determine an upper limit of 0.4 mJy, corresponding to an upper limit on the spectral index of $\alpha < -1.9$.

6.4. Discussion

Investigating the spectral index properties of distant radio halos is crucial to understand the mechanism of particle acceleration in these radio sources. So far, spectral studies in radio halos have been carried out starting from high-frequency observations (i.e. ∼ GHz), which were then followed up at lower frequencies. However, this approach tends to miss a large fraction of steep-spectra sources, simply because they are not detected in the GHz observations. This issue is particularly important for high-redshift clusters, as a large fraction of these halos, especially the low-mass systems, should have a steep spectral index ($\alpha < -1.5$, see Cassano & Brunetti, 2005; Cassano et al., 2006). This is due to the larger contribution of Inverse Compton energy losses (i.e. $dE/dt_{\mathrm{IC}} \propto (1+z)^4$) that is expected to hamper the acceleration of high-energy electrons. As a consequence, the ensuing synchrotron luminosity should be reduced. The increasing area of the LOFAR Two-Meter Sky Survey (LoTSS) will help avoid this bias towards flat-spectra halos. This survey at low frequencies is expected to observe a large number of previously undiscovered radio halos (e.g. Cassano et al., 2010a; van Weeren et al., 2020), which can be followed up at higher frequencies.

In Di Gennaro et al. (2021a) we presented the first statistical study of diffuse radio emission with LOFAR (120–168 MHz) of a sample of 19 distant ($z \geq 0.6$) galaxy clusters selected from the Planck SZ catalog (Planck Collaboration et al., 2016). In this work, we present a follow-up study at higher frequencies of the nine radio halos detected in the LOFAR observations. Our observations were carried out with the uGMRT, mainly at 550–900 MHz (Band 4), but for two clusters (i.e. PSZ2 G091.83+26.11 and PLCK G147.3–16.6) we also have observations at 250-550 MHz (Band 3). At these higher frequencies, we find the presence of diffuse radio emission in five of the nine clusters discovered in LOFAR. These are PSZ2 G091.83+26.11,

Table 6.4: Flux densities and largest linear sizes (LLS) of the radio halos in our sample.

Cluster name	S_{144} [mJy]	LLS_{144} [Mpc]	S_{400} [mJy]	LLS_{400} [Mpc]	S_{650} [mJy]	LLS_{650} [Mpc]	α_{650}^{144}
PSZ2 G086.93+53.18	5.6 ± 1.1	0.4–0.5	–	–	< 0.5	N/A	< -1.5
PSZ2 G089.39+69.36	10.0 ± 1.6	1.0	< 1.2	N/A	–	–	< -1.9
PSZ2 G091.83+26.11	65.4 ± 9.9	1.2	23.9 ± 2.0	1.2	14.5 ± 0.8	1.2	-1.00 ± 0.11
PSZ2 G099.86+58.45	18.1 ± 2.9	1.2	–	–	4.0 ± 0.4	1.0	-1.00 ± 0.13
PSZ2 G126.28+65.62	6.8 ± 1.1	0.8	–	–	< 0.5	N/A	< -1.6
PSZ2 G141.77+14.19	6.5 ± 1.2	0.6	–	–	1.2 ± 0.1	0.55	-1.12 ± 0.13
PLCK G147.3–16.6	21.0 ± 3.7	0.8	5.4 ± 0.6	1.0	2.8 ± 0.3	1.0	-1.34 ± 0.20
PSZ2 G147.88+53.24	8.2 ± 1.3	0.6	–	–	1.1 ± 0.2	0.5	-1.33 ± 0.17
PSZ2 G160.83+81.66	8.5 ± 1.5	0.7	–	–	< 0.4	N/A	< -1.9

The LOFAR flux densities agree within 1σ with the values reported in Di Gennaro et al. (2021a). The flux densities reported for PLCK G147.3–16.6 refer to the small halo region. For PSZ2 G089.39+69.36 the upper limit on the spectral index is calculated between 144 and 400 MHz.

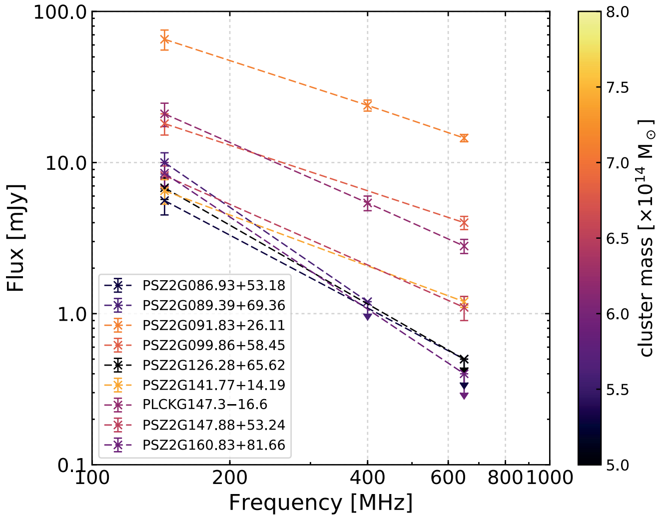

Figure 6.10: Radio spectra of the clusters in our sample (Table 6.4). The arrows show the upper limits on the fluxes.

PSZ2 G099.86+58+45, PSZ2 G141.77+14.19, PLCK G147.3–16.6 and PSZ2 G147.88+53.24. While we note that these clusters are also the most massive objects in our sample, with $M_{500,\mathrm{SZ}} \sim 6-8 \times 10^{14}$ M$_\odot$, the low-mass clusters in our sample (i.e. $M_{500,\mathrm{SZ}} = 5-6 \times 10^{14}$ M$_\odot$; PSZ2 G086.93+53.18, PSZ2 G089.39+69.36, PSZ2 G126.28+65.62 and PSZ2 G160.83+81.66), do not show diffuse radio emission at the uGMRT frequencies (Fig. 6.10).

For the uGMRT-detected radio halos, we measure integrated spectral indices between -1 and -1.3. These values are similar to what has been found for classical halos in local clusters (e.g Giovannini et al., 2009; Feretti et al., 2012; van Weeren et al., 2019). For the non-detections, given the upper limits on the flux densities obtained in the region covering the radio halo detected in LOFAR (see Tab. 6.4), we were able to determine an upper limits on the spectral index, being $\alpha < -1.5$. We also note that for those targets with three observing frequencies (PSZ2 G091.83+26.11 and PLCK G147.3–16.6), no spectral curvature is present. This means that the break frequency ν_s has to be at higher frequencies (i.e. $\nu_s > 650$ MHz). Hints of spectral steepening are indeed suggested with archival 1.4 GHz VLA observations of PSZ2 G099.86+58.45 (Cassano et al., 2019).

6.4.1. Comparison with theoretical models

Although our sample is not designed to test the occurrence of radio halos in high-redshift systems (because of its small size and low completeness), we can compare our results with model expectations. According to re-acceleration models, the possibility to detect diffuse radio emission depends on the break frequency ν_s of the synchrotron spectra. Therefore, halos can be observed only at $\nu \leq \nu_s$ with ν the observing frequency. Following the procedure in Cassano et al. (2019), we estimated the probability to form a radio halo as a function of the cluster mass, at a median redshift of $z = 0.7$, with a break frequency of $\nu_s \geq 140$ MHz and $\nu_s \geq 600$ MHz (see Fig. 6.11). The formation probability includes the cluster merger history (merger trees) the generation of turbulence, particle acceleration (including energy losses) and the resulting cluster synchrotron spectrum. In these models the turbulent energy, acceleration rate and magnetic field are considered constant in the halo volume (i.e. homogeneous models, Cassano et al., 2010a). Here we consider magnetic field strengths of 2 and 5 μGauss (solid and dashed lines in Fig. 6.11), which match the range of results in Di Gennaro et al. (2021a). The highest value on the magnetic field strength is set based on the value which maximises the lifetime of relativistic electrons at the system redshift, i.e. $B = B_{\rm CMB}/\sqrt{3}$ (where $B_{\rm CMB} = 3.25(1+z)^2$ μGauss is the magnetic field strength equivalent to that of the Cosmic Microwave Background). We assumed that the radio emission encompasses a region $R_H = 400$ kpc, i.e. the median size of the halos in our sample (see Tab. 6.4). The uncertainty of the estimated fraction of halos is obtained via 1000 Monte Carlo extractions of galaxy cluster samples from the pool of simulated merger trees (Cassano et al., 2010a, see red and yellow shaded areas in Fig. 6.11). We find that, in the mass interval of our sample $M_{500} = 5.0 - 8.0 \times 10^{14}$ M$_\odot$, and assuming $B = 5$ μGauss, the probability to observe a radio halo with steepening frequency $\nu_s \geq 140$ MHz is between the 60% and 30% (Fig. 6.11 red line), while it decreases down to 13–30% for $\nu_s \geq 600$ MHz (Fig. 6.11 yellow line), with a clear dependence on cluster mass. This agrees with our observations, where we detect a radio halo in about 50% of the total sample (9/19) at 144 MHz (Di Gennaro et al., 2021a) and in about 30% (5/19) at 650 MHz. The expected fractions of halos assuming $B = 2$ μGauss are consistent with the uncertainties given by the Monte Carlo simulations (see dashed lines in Fig. 6.11).

These expectations imply the presence of a population of ultra-steep spectra radio halos (USSRH) with $140 \leq \nu_s < 600$ MHz, which will be missed by observations at frequencies larger than 600 MHz, due to their ultra-steep radio spectra. In top panel of Fig.6.11, we show the fraction of these USSRH with respect to the total number of radio halos expected at 140 MHz, $f_{\rm USSRH}$, as a function of the cluster mass, assuming $B = 5$ μGauss and $B = 2$ μGauss (solid and dashed lines, respectively). Given the mass range of our clusters, i.e. $M_{500} = 5.0{-}8.0 \times 10^{14}$ M$_\odot$, we expect that 50–60% ($B = 5$ μGauss) or 65–60% ($B = 2$ μGauss) of these to be ultra-steep (i.e. $\alpha < -1.5$). Despite the low statistics, the estimate using higher magnetic fields is in good agreement with our observations, where we estimate 45–55% of USSRH (see Tab. 6.4). Increasing the number of distant radio halos will help in better determining the magnetic field levels in these clusters.

6.4.2. Occurrence of radio relics at high redshift

According to the predictions by Nuza et al. (2012), about 800 radio relics should have been observed at $0.5 < z < 1$ in the full LoTSS survey. However, Nuza et al. (2017) showed in a follow-up work that the majority of these relics, predicted in the simulations, would have small angular extensions ($\lesssim 2'$ when the image is smoothed with a 45" beam). If such a population of relics does exist, it would be challenging to recognise the corresponding radio features in surveys like LoTSS and classify them correctly. The results by Nuza et al. (2017) indicate that relics as extended as the one in PSZ2 G091.83+26.11 and sufficiently bright to be detected are rare in distant clusters.

In our total sample of 19 clusters at $z \geq 0.6$ we found one candidate radio relic, in PSZ2 G091.83+26.11. This source has a linear size larger than 1 Mpc. Although our sample is not complete and is rather small, we are likely observing the most violent mergers in the distant Universe (i.e. $M > 5 \times 10^{14}$ $M_\odot$) and we would have expected to detect more relics. At $z > 0.5$, five additional radio relics, namely PLCK G004.5-19.5 ($z = 0.52$, DEC $= -33°$, Albert et al., 2017), MACS J1149.5+2223 ($z = 0.544$, Bonafede et al., 2012, Bruno et al., subm.), MACS J0717.5+3745 ($z = 0.546$, Bonafede et al., 2014; Rajpurohit et al., 2021), MACS J0025.4-1222 ($z = 0.584$, DEC $= -12°$, Riseley et al., 2017), ACT-CL J0102-4915 ("el Gordo"; $z = 0.87$, DEC $= -49°$; Lindner et al., 2014), and two candidate radio relics, namely ACT-CL J0014.9-0057 ($z = 0.533$, DEC $= -1°$, Knowles et al., 2019) and ACT-CL J0046.4-3912 ($z = 0.592$, DEC $= -39°$, Knowles et al., 2021) are known in the literature[2]. Among these, MACS J0717.5+3745, MACS J1149.5+2223 and ACT-CL J0046.4-3912 host relics with linear sizes of about 1 Mpc. The small number of detections available to date does not allow a clear comparison with the current models. Despite that, the findings we present in this paper will be crucial to develop more stringent predictions on the magnetic properties of the ICM at the location of the shock, acceleration efficiency and seed populations when the first structure formed (Brüggen & Vazza, 2020).

6.5. Conclusions

In this paper, we presented follow-up observations of the high-redshift Planck-SZ clusters hosting diffuse radio sources presented in Di Gennaro

[2] Only MACS J1149.5+2223 and MACS J0717.5+3745 are observed with LOFAR.

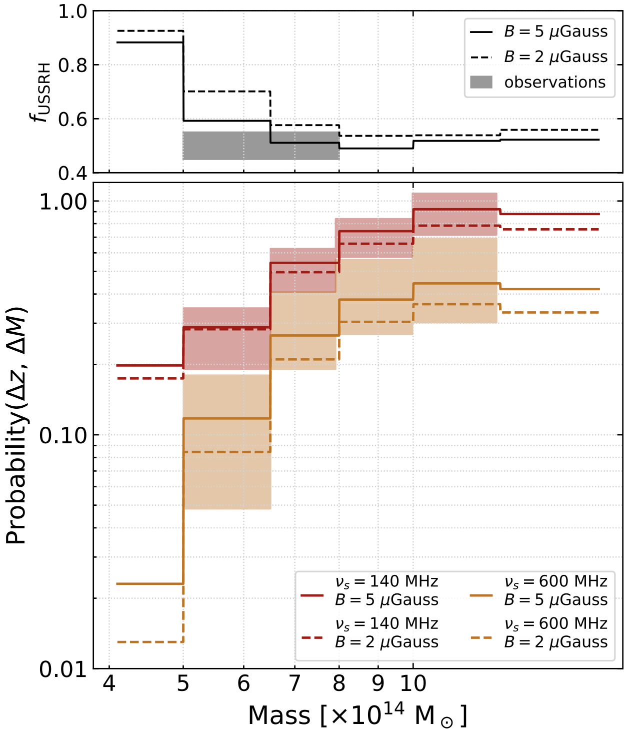

[h!]

Figure 6.11: Probability of forming radio halos with $\nu_s > 140$ and $\nu_s > 600$ MHz (red and yellow lines, respectively) as a function of the cluster virial mass in the redshift range 0.6-–0.7. Magnetic fields of $B = 5$ μGauss and $B = 2$ μGauss are assumed (solid and dashed lines, respectively). The shadowed regions represent the 1σ uncertainty derived through Monte Carlo calculations. Top panel: Expected fraction of USSRH visible at 144 MHz with steepening frequency $\nu_s < 600$ MHz as a function of the cluster virial mass, assuming $B = 5$ μGauss and $B = 2$ μGauss (solid and dashed lines, respectively). The shadowed area indicates the observed fraction of USSRH in our sample.

et al. (2021a). Our observations were taken with the upgraded GMRT (uGMRT) in Band 4 (550–900 MHz) and, for two clusters (i.e. PSZ2 G091.83+26.11 and PLCK G147.3–16.6) also in Band 3 (250–500 MHz)[3]. These observations were combined with LOFAR data at 144 MHz. Below we summarise our findings.

- About the 50% (5/9) of the clusters presented show the presence of a radio halo in the uGMRT observations, up to $\nu = 650$ MHz.

- For these systems, we measure integrated spectral indices between -1 and -1.4. We note that these clusters are also the most massive in our sample, and at these redshifts ($M > 6 \times 10^{14}$ $M_{\odot}$), which imply also more energetic merger events.

- For the clusters that host a radio halo in the LOFAR images but are not detected in the uGMRT ones, we estimate upper limits on the spectral indices of $\alpha < -1.5$, in line with the predictions of re-acceleration models (Cassano et al., 2010a).

- Although our sample is not complete, the fraction of cluster hosting halos and the spectral indices agree with the expectations from theoretical models of re-acceleration (Cassano & Brunetti, 2005; Cassano et al., 2006, 2010a).

- We find only one candidate radio relic in this sample of distant clusters, in PSZ2 G091.83+26.11. This is possibly contaminated by a double radio galaxy, although no optical counterparts have been observed in the PanSTARRS data. Future polarisation analysis with the VLA will provide further information on the nature of this radio source.

Observing distant diffuse radio emission is crucial for the investigation of the magnetic field evolution over cosmic time, and Universe magnetogenesis. Given the small size of the sample presented in this work, comparison with cosmological simulations are difficult. Upcoming observations with the X-ray satellite eROSITA (Extended Roentgen Survey Imaging Telescope Array; Merloni et al., 2012, 2020) will help find new distant galaxy clusters, that can be easily followed up with radio low-frequency observations.

Acknowledgements: This paper is based on data obtained with the Giant Metrewave Radio Telescope (GMRT). GMRT is run by the National Centre for Radio Astrophysics of the Tata Institute of Fundamental Research. The National Radio Astronomy Observatory is a facility of the National

[3] PSZ2 G089.39+69.36 was observed only in Band 3.

Science Foundation operated under cooperative agreement by Associated Universities, Inc. We thank the staff of the GMRT that made these observations possible. This manuscript is based on data obtained with the International LOFAR Telescope (ILT). LOFAR (van Haarlem et al. 2013) is the Low Frequency Array designed and constructed by ASTRON. It has observing, data processing, and data storage facilities in several countries, which are owned by various parties (each with their own funding sources), and which are collectively operated by the ILT foundation under a joint scientific policy. The ILT resources have benefited from the following recent major funding sources: CNRS-INSU, Observatoire de Paris and Université d'Orléans, France; BMBF, MIWF-NRW, MPG, Germany; Science Foundation Ireland (SFI), Department of Business, Enterprise and Innovation (DBEI), Ireland; NWO, The Netherlands; The Science and Technology Facilities Council, UK; Ministry of Science and Higher Education, Poland; The Istituto Nazionale di Astrofisica (INAF), Italy. This research made use of the Dutch national e-infrastructure with support of the SURF Cooperative (e-infra 180169) and the LOFAR e-infra group. The Jülich LOFAR Long Term Archive and the German LOFAR network are both coordinated and operated by the Jülich Supercomputing Centre (JSC), and computing resources on the supercomputer JUWELS at JSC were provided by the Gauss Centre for Supercomputing e.V. (grant CHTB00) through the John von Neumann Institute for Computing (NIC). This research made use of the University of Hertfordshire high-performance computing facility and the LOFAR-UK computing facility located at the University of Hertfordshire and supported by STFC [ST/P000096/1], and of the Italian LOFAR IT computing infrastructure supported and operated by INAF, and by the Physics Department of Turin university (under an agreement with Consorzio Interuniversitario per la Fisica Spaziale) at the C3S Supercomputing Centre, Italy.The National Radio Astronomy Observatory is a facility of the National Science Foundation operated under cooperative agreement by Associated Universities, Inc. GDG and RJvW acknowledge support from the ERC Starting Grant ClusterWeb 804208. HJAR acknowledge support from the ERC Advanced Investigator programme NewClusters 321271. AB and RJvW acknowledge support from the VIDI research programme with project number 639.042.729, which is financed by the Netherlands Organisation for Scientific Research (NWO). VC acknowledges support from the Alexander von Humboldt Foundation.

.1. Optical-Radio overlays for PSZ2 G091.83+26.11

Here we present the optical *irg* image of PSZ2 G091.83+26.11, taken from the PanSTARRS archive[4] (Chambers et al., 2016). We overlay the

[4] `https://ps1images.stsci.edu/cgi-bin/ps1cutouts`

radio contours of the uGMRT 650 MHz image, after removing the contribution of the halo emission, to investigate possible optical counterparts that generate the radio emission of the candidate radio relic.

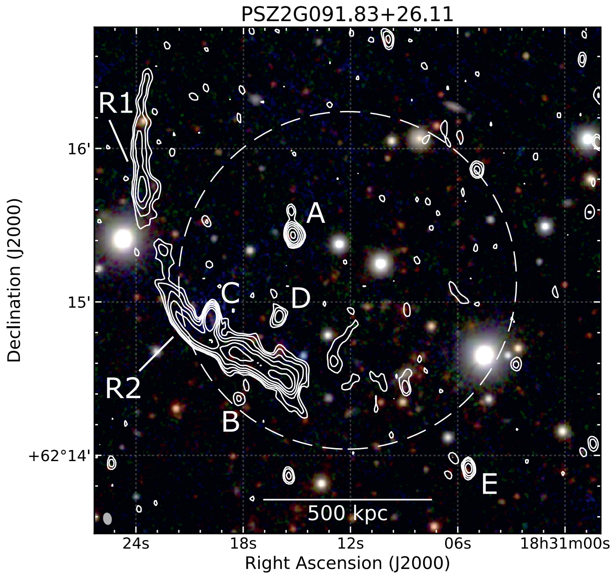

Figure .1.12: PanSTARRS optical *irg* image of PSZ2 G091.83+26.11. Radio contours at 650 MHz without the contribution of the radio halo (i.e. with the *uv*-cut at 500 kpc) are overlaid in white. The white dashed circle represents R_{500} region. Labels follow Fig. 6.3.